Electromechanical Measurements and Modeling of a High-Performance Small-Area Ultra-Thin SOI MEMS Piezoresistive Pressure Sensor

Xi Zeng, Nicolas André, *Member, IEEE*, Eléonore Masarweh, Ottilie Bonfanti, and Denis Flandre, *Senior Member, IEEE*

***Abstract*— A microelectromechanical system (MEMS) silicon-on-insulator (SOI) differential pressure sensor, integrating a Wheatstone full bridge with four thin monocrystalline Si mesa piezoresistors located at the edges of an ultrathin (2.5 μm) and miniaturized (0.18 mm^2) Si_3N_4/SiO_2 membrane, is thoroughly investigated by both electrical and mechanical measurements. A comprehensive model is proposed to analyze the physical phenomena and correlate the electrical and mechanical properties. The pressure sensor demonstrates excellent electrical and mechanical performances under positive backside differential pressure, that is, for upward deflection, at supply voltages of 5 and 10 V. Under 10 V, the output voltage exhibits a linear increase from 0 to 100 kPa, achieving a high sensitivity and a mechanical figure of merit of 0.461 μV/V/Pa and 2.56 ppm/Pa/mm^2, respectively, with a full-scale (FS) total nonlinearity error (NL) up to 0.78% FS. Analyzing the topographic measurements by deflection-pressure and stress-strain methods, Young's modulus and residual stress are extracted to be ~116 GPa and 82 MPa, respectively. According to a comprehensive model, the optimal electrical performance of the pressure sensor is attributed to a high strain increase with pressure thanks to an ultrathin miniaturized membrane and piezoresistors closer to the membrane bottom surface. The relatively high total nonlinearity is caused by a dominant mechanical nonlinearity, which can be reduced in the future by improving the gauge positions and alignment.**

***Index Terms*— Comprehensive modeling, electrical measurement, microelectromechanical system (MEMS), piezoresistive pressure sensor, silicon-on-insulator (SOI) technology, topographic measurement.**

I. Introduction

MICROELECTROMECHANICAL system (MEMS) sensors integrating mechanical and electrical components are among the most widely used sensors in commercial and industrial applications to precisely detect physical quantities, such as pressure, temperature, acceleration, magnetic field [1], [2]. Thanks to the rapid development of silicon micromanufacturing technologies, MEMS pressure sensors composed of a diaphragm and a transducer share the highest sales volume in the sensor market [3], [4]. The great potential of MEMS pressure sensors is well established in various domains, such as aerospace, automotive industry, biomedical equipment, portable electronic devices, process control [5], [6], [7], [8]. Considering different transduction mechanisms, Si-based MEMS piezoresistive pressure sensors were first developed and mostly commercialized thanks to their high sensitivity, low nonlinearity, low cost, high efficiency, small size, low-power consumption, high mechanical and electrical stability, and great potential to be mass manufactured in the industry [9], [10]. However, most of the previously reported articles focused on either electrical or mechanical measurements without connecting the electrical and mechanical performances of pressure sensors.

To design high-performance piezoresistive pressure sensors, the Wheatstone bridge is a preferred electrical configuration with stable output signals [11]. Regarding the mechanical design of pressure sensors, the shape, thickness, and area of the surface-micromachined diaphragms need to be carefully considered [12], [13]. Pressure sensors with reduced diaphragm areas enable micro-scale integration in applications such as MEMS-based microfluidics systems (e.g., microneedles, micropumps and microreservoirs) [14], [15] but can result in lower sensitivity [16], [17], [18]. According to the mechanical behaviors of flat diaphragms, the sensitivity can be improved by reducing the residual stress and enhancing the width to thickness ratio of the diaphragm [13]. Decreasing the diaphragm thickness can thus overcome the problem induced by a smaller diaphragm area, but it would deteriorate the nonlinearity of the pressure sensor [9]. Implanting Si planar piezoresistors in traditional pressure sensors, the Si layer does not only serve to implement the active piezoresistors but also as part of the membrane stack. Therefore, Si cannot be fully etched, limiting the final diaphragm thickness to between 10 and 20 μm [6], [9], [16], [19]. Based on bulk silicon technology, a pressure sensor integrating a Si/SiO_2 diaphragm with an area and a thickness of ~0.23 mm^2 and 13.8 μm resp. exhibits a sensitivity of 0.096 μV/V/Pa and a nonlinearity error (NL) of 0.16% Full-scale (FS) [16]. Another thick silicon-on-insulator (SOI) pressure sensor featuring a Si diaphragm with an area and a thickness of ~0.3025 mm^2 and 14 μm exhibits a sensitivity of 0.14 μV/V/Pa [6]. Further reducing the diaphragm thickness to less than 10 μm by integrating Si mesa piezoresistors in bulk silicon technology, a pressure sensor with a diaphragm area and thickness of ~0.09 mm^2

Received 14 October 2024; revised 13 March 2025; accepted 17 April 2025. Date of publication 5 May 2025; date of current version 15 May 2025. This work was supported in part by the 4Equip Wallonia Project of Belgium under Grant 8168 and in part by the Stochastic Spiking Wireless Multimodal Sensory Systems (SWIMS) European Research Council (ERC) Synergy Project under Grant 101119062. The Associate Editor coordinating the review process was Dr. Bin Zi. *(Corresponding author: Xi Zeng.)*

The authors are with the Institute of Information and Communication Technologies, Electronics and Applied Mathematics, UCLouvain, 1348 Ottignies-Louvain-la-Neuve, Belgium (e-mail: xi.zeng@uclouvain.be).

Digital Object Identifier 10.1109/TIM.2025.3566836

1557-9662 © 2025 IEEE. All rights reserved, including rights for text and data mining, and training of artificial intelligence and similar technologies. Personal use is permitted, but republication/redistribution requires IEEE permission.
See https://www.ieee.org/publications/rights/index.html for more information.
Authorized licensed use limited to: Univ Catholique de Louvain/UCL. Downloaded on October 27,2025 at 12:44:51 UTC from IEEE Xplore. Restrictions apply.

and 2 μm shows a sensitivity of 0.0548 μV/V/Pa and a NL of 0.1% FS [20]. However, these reported sensors integrating either SOI technology or mesa piezoresistors on thick Si layers may exhibit a high leakage current, which can be reduced by integrating mesa piezoresistors in SOI technology. Introducing stress concentrators in the pressure sensor is another way to improve the sensitivity and linearity and reduce the hysteresis effect [21], [22]. Previously reported works were based on the classical figures of merit (FoM), while in [23], new electrical and mechanical FoMs for small-size pressure sensors were introduced to ease and objective comparisons of sensors with different designs and technologies.

This work introduces a high-performance SOI MEMS Wheatstone-bridge piezoresistive pressure sensor: By fully etching the bulk Si, we achieved one of the thinnest reported small-area Si_3N_4/SiO_2 membrane combining the benefits of both monocrystalline Si mesa piezoresistors and SOI technology. The resistors were placed closer to the membrane bottom surface to have a higher bending-induced strain under the backside positive pressure. First, in Section IV-B, the electrical characteristics of the pressure sensor are investigated under both negative and positive pressure considering the FoMs of [23]. Second, in Section IV-C, the mechanical properties of the Si_3N_4/SiO_2 membrane are extracted and thoroughly analyzed by topography measurements. Finally, in Section IV-D, we propose a comprehensive model to explain and link the physical phenomena observed in both electrical and mechanical measurements.

II. Sensor Structure and Fabrication Details

The top-viewed photograph of the fabricated SOI piezoresistive pressure sensor was obtained by an optical microscope (Zeiss Axio Imager Vario) in Fig. 1(a). Four monocrystalline p-type Si piezoresistors were defined with active areas of 40 $\times$ 15 μm^2, a thickness of 1 μm and an average hole concentration of about 7 $\times$ 10^{16} cm^{-3} in the active piezoresistive part to achieve resistance values of $\sim$7.1 kΩ. To optimize the Si piezoresistive coefficients, a hole concentration below 10^{18} cm^{-3} is recommended, otherwise, the coefficient would be significantly reduced [24]. Among the piezoresistors, two transverse resistors $R_\perp$ [R_1 and R_3, with the scanning electron microscope (SEM) image shown in Fig. 1(b)], are located close to the left and right edges of the diaphragm, while two longitudinal resistors $R_\parallel$ [R_2 and R_4, with the SEM image shown in Fig. 1(c)] are located at the top and bottom edges. The diaphragm has an area of 0.18 mm^2 with a total thickness of 2.5 μm composed of 1.5 μm Si_3N_4 and 1 μm SiO_2. The octagonal shape allows to optimize the access pad positions for minimizing the full die area (down to 1 mm^2) toward applications that require such small-scale aspect ratio.

The Si piezoresistive pressure sensor was fabricated on a SOI wafer, featuring a 500 nm buried SiO_2 (BOX), a 1 μm p-type (100) Si overlayer and a 280 μm bulk Si after grinding. Fig. 2 shows the cross-sectional schematics for the main successive fabrication steps of the pressure sensor represented along the red dashed line in Fig. 1. All the patterning steps were carried out by positive optical lithography in Suss MA6 mask aligner with a resolution of 1 μm.

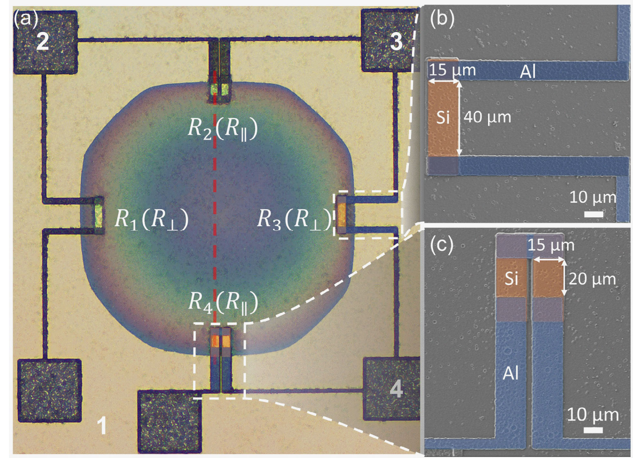

Fig. 1. (a) Top-viewed optical microscope photograph of a fabricated SOI piezoresistive Wheatstone-bridge pressure sensor with an ultrathin (2.5 μm) and miniaturized (0.18 mm^2) octagonal diaphragm. Access pads are numbered 1 to 4. Access 1 consists of 2 pads that can be short-circuited or used separately for bridge calibration and offset suppression. SEM images of (b) transverse and (c) longitudinal piezoresistors (the orange and blue areas depict Si and Al layers, respectively).

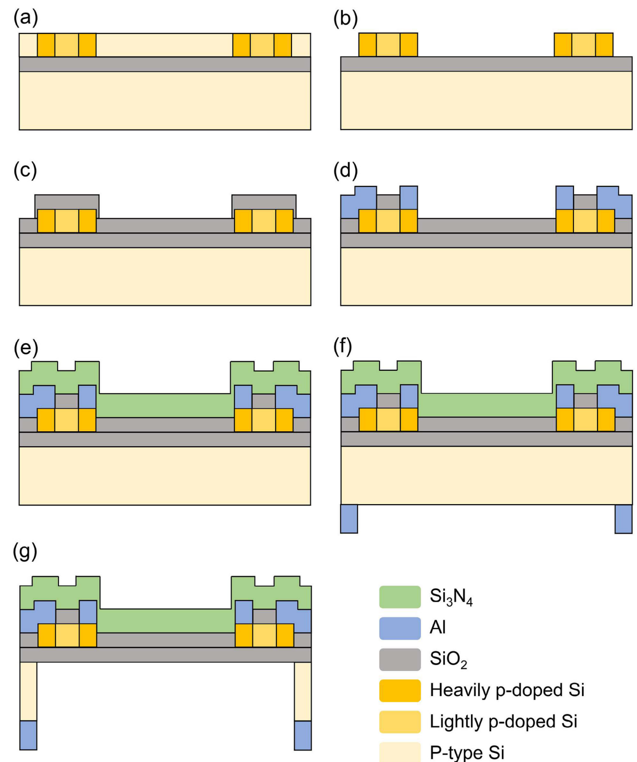

Fig. 2. Cross-sectional schematics (not at scale) illustrating the successive fabrication process steps of the Si piezoresistive pressure sensor, along the red dashed line in Fig. 1(a). (a) Boron doping in SOI substrate. (b) Si RIE. (c) SiO2 PECVD. (d) Al/Si sputtering. (e) Si3N4 PECVD. (f) Al evaporation. (g) Si DRIE.

1) The piezoresistors were patterned and doped by surface boron implantations at energies of 20 keV, with doses of 5 $\times$ 10^{13} and 5 $\times$ 10^{15} cm^{-2} for lightly and heavily doped regions corresponding to their active sensing parts and ohmic contacts, respectively [see Fig. 2(a)].
2) The piezoresistors were mesa patterned by reactive ion etching (RIE) of the Si overlayer [see Fig. 2(b)].

Authorized licensed use limited to: Univ Catholique de Louvain/UCL. Downloaded on October 27,2025 at 12:44:51 UTC from IEEE Xplore. Restrictions apply.

3) SiO_2 layers with a total thickness of 500 nm were next deposited by plasma-enhanced chemical vapor deposition (PECVD) in Oxford Plasmalab 100 [see Fig. 2(c)].
4) Vias were patterned in the top SiO_2 by BHF etching. A 1.3 μm Al/Si(1%) layer was sputtered and patterned to contact the resistors with the interconnect lines and the input/output access pads to the bridge [see Fig. 2(d)]. An annealing at 432 °C for 30 min in forming gas was performed to ensure ohmic contacts between Si and Al.
5) A tensile 1.5 μm Si_3N_4 layer was deposited by PECVD in Oxford Plasmalab 100 to balance the compressive stress of the SiO_2 layers and target a flat low-stress membrane after release, as well as to passivate the top surface of the pressure sensor [see Fig. 2(e)]. The Si_3N_4 layer was patterned by CHF_3/SF_6 plasma in Oxford Plasmalab 100 to open the Al access pads.
6) An Al hard mask (for the subsequent substate micromachining) was e-beam evaporated at the backside of the wafer and patterned by H_3PO_4 wet etching [see Fig. 2(f)].
7) The membrane was finally released by deep RIE (DRIE, e.g., BOSCH process with SF_6/C_4F_8 cycles) in Oxford Plasmalab 100 [see Fig. 2(g)]. The BOX layer is considered as an accurate etch-stop layer for the dry etching of the bulk Si.

III. Package and Measurement Setups

After the wafer-level fabrication, individual chips of $\sim$1 mm^2 were diced by diamond saw and glued by cyanoacrylate glue on a printed circuit board (PCB) as shown in the insets of Fig. 3(a). The membrane with a diameter of 490 μm was optically aligned with a hole opened by a drill with a diameter of 0.6 mm in the center of the PCB to allow differential pressure control. The access pads were bonded with the Cu contacts of the PCB by Au wires with a diameter of 20 μm.

As shown in Fig. 3(a) and (b), the PCB was then placed in a pressure vessel, where differential pressures can be applied, with regards to the ambient air, on the backside of the membrane using the KAL 100 pressure calibration device (Halstrup–Walcher GmbH). Positive or negative backside pressure with regards to the ambient pressure on top of the chip leads to upward or downward membrane deflections, respectively. The pressure leakage of the measurement system was measured to be small enough to be neglected thanks to the excellent airtightness of the whole assembly.

The electrical and mechanical measurement setups for the pressure sensor are shown in Fig. 3(a) and (b), respectively. After soldering connectors and electrical wires to the PCB Cu contacts, electrical measurements were carried out at room temperature in a dark chamber, using 4 high-precision source measure units (SMUs) of a Keithley 4200-SCS semiconductor characterization system. Three-dimensional topographies of the pressure sensor under different applied pressures were monitored by a Polytec MSA-500 Micro System Analyzer in the dark. This topography measurement system detects the fringe patterns of the interference between the light reflected from the reference and the test sample and saves

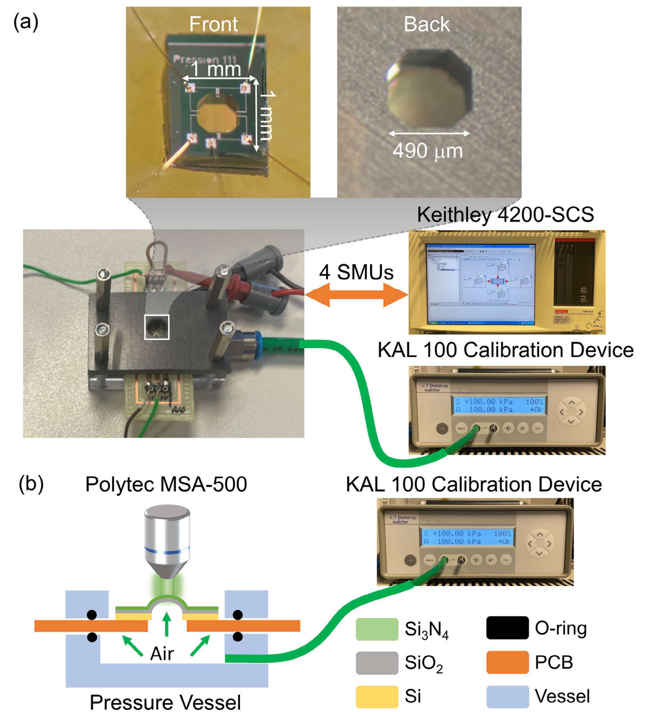

Fig. 3. (a) Electrical and (b) mechanical measurement setups for the Si piezoresistive pressure sensor. The top insets in (a) show the front and backsides of the wire-bonded sensor on PCB.

equivalent z-coordinate of the sample. Additionally, the electrical current-voltage characteristics of the Wheatstone bridge were measured by an Agilent B1500A semiconductor device analyzer in an MPI TS3000-SE semiautomated probe system.

IV. Results and Discussion

A. Theory of Wheatstone Bridge

Piezoresistive pressure sensors are indirect transducers, composed of a diaphragm and piezoresistive strain gauges. A mechanical membrane deformation caused by the applied differential pressure is converted into electrical signals in the strain gauges. The strain gauges are generally silicon piezoresistors implanted in bulk Si or SOI technology. The piezoresistive coefficient (π) includes the directional changes of electrical resistivity and mechanical stress [25]. For silicon with cubic symmetry, the π coefficient is composed of three components: π_{11} and π_{12} for stresses applied longitudinally and transversally to the current direction, and π_{44} for the stress applied in shear with the current direction [26]. For [110] direction on p-type lightly doped (100) silicon, longitudinal ($\pi_{\parallel}$) and transverse ($\pi_{\perp}$) piezoresistive coefficients are estimated by $\pi_{\parallel} = (\pi_{11} + \pi_{12} + \pi_{44})/2 = 718$ TPa^{-1} and $\pi_{\perp} = (\pi_{11} + \pi_{12} - \pi_{44})/2 = -663$ TPa^{-1}, respectively [23].

In Fig. 4(a), to measure the resistance variation precisely, a Wheatstone full-bridge structure is implemented. Once a supply voltage V_{dd} is applied between Nodes 1 and 3, an output voltage V_o depending on the ratios of the resistances (e.g., R_1:R_2 and R_3:R_4) would be detected between nodes 2 and 4. Ideally, if the resistors have identical values at 0 kPa, a voltage equal to $V_{dd}/2$ is measured at nodes 2 and 4. However, due to the fabrication imprecision, the pairs of transverse and longitudinal resistors are not perfectly identical.

Authorized licensed use limited to: Univ Catholique de Louvain/UCL. Downloaded on October 27,2025 at 12:44:51 UTC from IEEE Xplore. Restrictions apply.

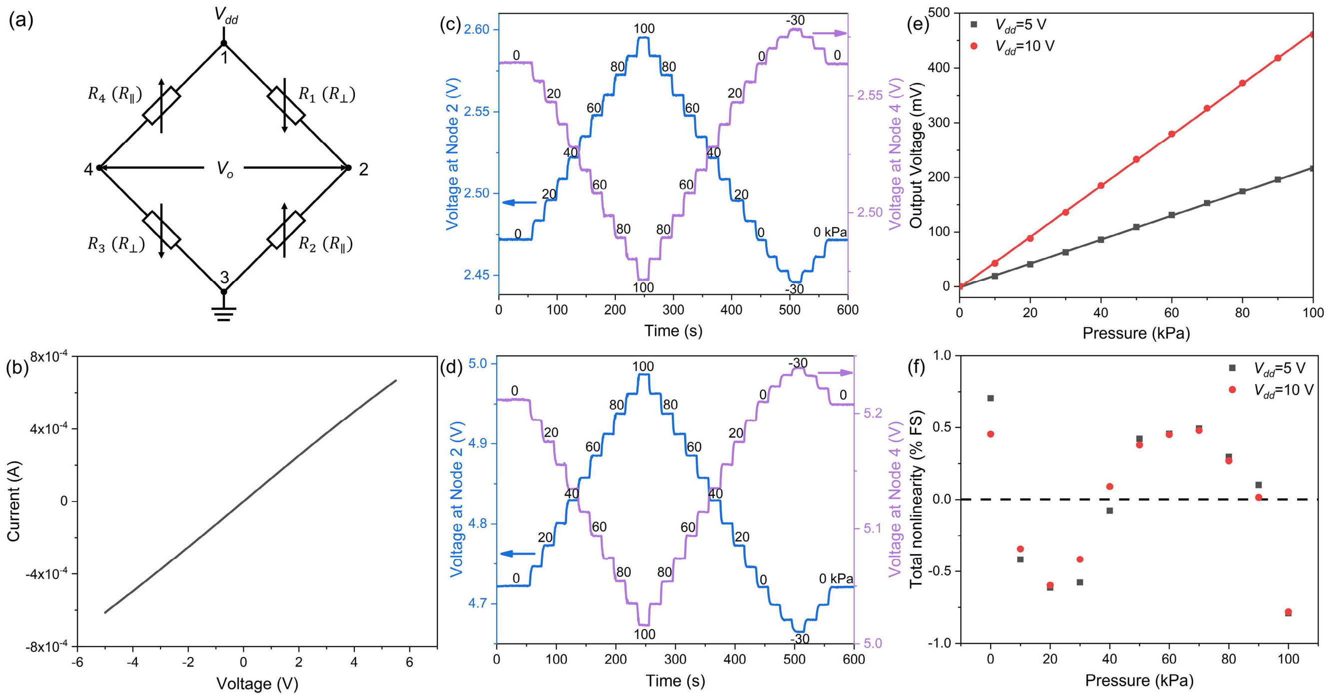

Fig. 4. (a) Wheatstone full-bridge structure, where nodes 1 to 4 correspond to the access pads 1 to 4 presented in Fig. 1. (b) Current–Voltage curve of the Wheatstone full bridge from -5 to 5 V at zero applied pressure. Voltage-time curves of the Si piezoresistive pressure sensor under varying backside differential pressure between -30 and 100 kPa, with (c) $V_{dd} = 5$ V and (d) $V_{dd} = 10$ V, respectively. (e) Output voltage (dots are measured data, lines are linear fittings) and (f) total nonlinearity error of the pressure sensor between 0 and 100 kPa with $V_{dd} = 5$ and 10 V, respectively.

Therefore, a systematic offset has appeared and the sum of the two voltages at nodes 2 and 4 is not equal to V_{dd}. When the membrane deflects under differential pressure, $\sigma_\parallel$ and $\sigma_\perp$ are the longitudinal and transverse stresses that occur in perpendicular and parallel to the membrane edge. The strain gauge pairs including two $R_\perp$ and two $R_\parallel$ experience either negative or positive resistance variations [23]

$$R_\parallel = R_0\left(1 + \pi_\parallel\sigma_\parallel + \pi_\perp\sigma_\perp\right) \tag{1}$$
$$R_\perp = R_0\left(1 + \pi_\parallel\sigma_\perp + \pi_\perp\sigma_\parallel\right) \tag{2}$$

where R_0 is the resistance without applied pressure. In compliance with the Kirchhoff's laws, the corresponding output voltage V_o with piezoresistance variations induced by an applied pressure is written as follows [27]:

$$V_o = \frac{R_\parallel - R_\perp}{R_\parallel + R_\perp} V_{dd} = \frac{\left(\pi_\parallel - \pi_\perp\right)\left(\sigma_\parallel - \sigma_\perp\right)}{2 + \left(\pi_\parallel + \pi_\perp\right)\left(\sigma_\parallel + \sigma_\perp\right)} V_{dd}. \tag{3}$$

Considering slight differences in the pairs of resistors $R_\parallel$ and $R_\perp$, the output voltage at 0 kPa is not zero and this systematic offset should be subtracted as follows:

$$V_o = |V_4(p_i) - V_4(0)| + \left|V_2\left[p_i\right] - V_2[0]\right| \tag{4}$$

where V_2 and V_4 are voltages at nodes 2 and 4 under a pressure of p_i or 0 kPa, respectively.

B. Electrical Measurements

Sensitivity (S) and NL are two critical FoM to quantitify the electrical performance of pressure sensors. By removing the influence of the supply voltage, the normalized S, which evaluates the ability to convert mechanical pressure inputs into electrical outputs, is defined as the slope of the output voltage versus pressure [28]

$$S = \frac{\partial V_o}{V_{dd} \cdot \partial p}. \tag{5}$$

Further mitigating the effect of the membrane area (here $A \approx 0.18$ mm^2), a mechanical figure of merit (FoM$_m$) is calculated as in [23]

$$\mathrm{FoM}_m = S/A. \tag{6}$$

NL is defined as the deviation of the output values between each measured point and the ideal linear curve [27]

$$\mathrm{NL}_{T,M} = 100\% \times \frac{V_o(p_i) - V_{\mathrm{of}}(p_i)}{y_{\mathrm{FS}}} \tag{7}$$
$$\mathrm{NL}_E = 100\% \times \frac{I_o - I_{\mathrm{of}}}{y_{\mathrm{FS}}} \tag{8}$$

where $V_o(p_i)$ and $V_{\mathrm{of}}(p_i)$ are the measured and fit output voltages at a pressure of p_i, I_o, and I_{of} are the measured and fit output currents, and y_{FS} is the corresponding FS output. The maximum error value is the nonlinearity of the pressure sensor in [%FS]. NL$_T$ denotes the total NL of the sensor including both electrical NL (NL$_E$) of the resistors in the Wheatstone bridge and mechanical NL (NL$_M$) of the membrane deformation. Current–Voltage (I–V) curve of the full bridge between nodes 1 and 3 was measured without applied pressure from -5 to 5.5 V in Fig. 4(b). Considering a maximum working voltage range of $\sim$0.5 V around 5 V under pressure operation, NL$_E$ of the full bridge is calculated to be less than 0.25% FS from 4.75 to 5.25 V.

Voltage versus time curves of the as-fabricated pressure sensor, measured under V_{dd} of 5 and 10 V with varying

Authorized licensed use limited to: Univ Catholique de Louvain/UCL. Downloaded on October 27,2025 at 12:44:51 UTC from IEEE Xplore. Restrictions apply.

pressure, are obtained in Fig. 4(c) and (d), respectively. Due to fabrication variations, the pairs of transverse and longitudinal resistors are not perfectly identical, resulting in the sum of the voltages at nodes 2 and 4 to be unequal to the supply voltage. To stabilize the measurement system, the pressure sensor was first measured without any applied pressure for about 50 s. The differential pressure then applied on the backside of the membrane increased from 0 to 100 kPa, next decreased to −30 kPa and finally returned to 0 kPa, with a variation step of 10 kPa and a duration of about 20 s for each step. Once the pressure is stabilized, no airflow occurred in the pressure vessel. Considering the limited membrane deformation, the applied pressure on the membrane keeps fairly uniform.

With varying backside differential pressure, V_{N2} and V_{N4} accordingly change due to the piezoresistance variations. When a positive pressure of 100 kPa is applied at V_{dd} of 5 and 10 V, V_o of 216 and 461 mV are obtained, corresponding to S of 0.432 and 0.461 μV/V/Pa and FoM_m of 2.4 and 2.56 ppm/Pa/mm^2, respectively. A higher V_{dd} is preferred to increase sensitivity and accuracy when measuring small resistance changes in the Wheatstone bridge, but it increases the risk to damage the circuit. As illustrated in Fig. 4(e), V_o increases linearly with the rising positive pressure, indicating an almost constant sensitivity. The calculated NL_T in Fig. 4(f) are either positive or negative but remain low. The maximum NL_T of the pressure sensor under positive pressure are 0.79% FS and 0.78% FS extracted at 100 kPa for V_{dd} of 5 and 10 V, respectively. As NL_T is measured to be mostly unrelated to the operating voltage of the bridge and much larger than the electrical NL_E, NL_M will be further studied in Sections IV-C and IV-D.

On the other hand, as the negative pressure increases from 0 to −30 kPa, V_o exhibits reduced linearity, with the rate of V_o change decreasing from 35 mV between 0 and −10 kPa, to 18 mV between −20 and −30 kPa (V_{dd} = 10 V). Further increasing the pressure over −30 kPa, no more significant output signal was detected. When a negative pressure of −30 kPa is applied, the obtained V_o values are 42 and 85 mV, corresponding to S of 0.28 and 0.283 μV/V/Pa and FoM_m of 1.56 and 1.57 ppm/Pa/mm^2 for $V_{dd} = 5$ and 10 V, respectively. The maximum NL_T of the pressure sensor under negative pressure is calculated to be 4.1% FS and 4% FS under a pressure of −10 kPa for V_{dd} = 5 and 10 V, respectively. Considering the poor electrical performance under negative pressure, the following mechanical analyses will focus on the positive pressure range thoroughly, but an explanation for the limited performance in the negative pressure range will be given in Section IV-D.

C. Mechanical Measurements

Mechanical measurements were next carried out, showing in Fig. 5 the 3-D topographies of the Si_3N_4/SiO_2 membrane without external pressure and at positive backside differential pressures of 30, 70, and 100 kPa, respectively. Without backside pressure in Fig. 5(a), the membrane appears almost flat, with a maximum membrane height difference of ~0.47 μm (Fig. 6) between the center (x = 245 μm) and the edge ($x = 0$ μm). Such an initial membrane height is induced by the external forces generated during the processing, gluing, wire bonding, and packaging. When a positive backside pressure is applied, the membrane undergoes an upward deflection, with significant increases at higher pressures, such as 100 kPa in Fig. 5(d) compared to 30 and 70 kPa in Fig. 5(b) and (c). Considering a symmetrical distribution of the membrane deflections in all directions shown in Fig. 5, the deflection profiles of the membrane under varying differential pressure from −30 to 100 kPa with a step of 10 kPa are given in Fig. 6. These curves are extracted along the radius directions of the topographies and fit by second-order polynomials [29]. The noisy fluctuations observed in these curves are attributed to some artifacts of the Polytec MSA-500 based on fringe projection and possible reflections inside the membrane. Especially at the edges where the membrane is not flat, the curves become noisier due to less predictable reflections, leading to increased variabilities and irregularities in the fringe patterns.

As can be seen in Fig. 1, the membrane radius is 245 μm, while the average distance from the resistor centers to the membrane edges is 23 μm. Such an offset is determined by a safe alignment margin of 10 μm in the device design, a slight misalignment of the backside lithography and a slight

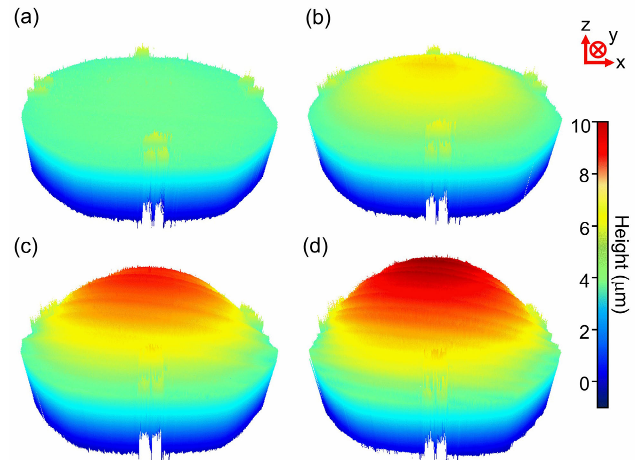

Fig. 5. 3-D topographies of Si_3N_4/SiO_2 membrane at (a) 0, (b) 30, (c) 70, and (d) 100 kPa. Darker red or blue color represents a higher- or lower-upward deformation of the membrane, respectively.

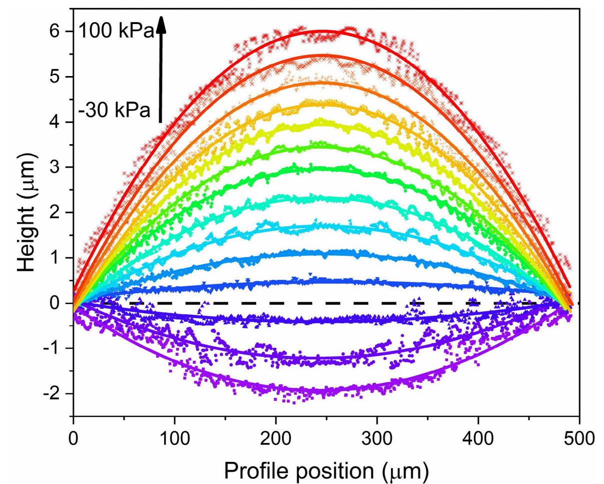

Fig. 6. Deformation profiles of Si_3N_4/SiO_2 membrane under varying differential pressure from −30 to 100 kPa, with a step of 10 kPa (the dots are measured data, and the lines are second-order polynomial fittings).

Authorized licensed use limited to: Univ Catholique de Louvain/UCL. Downloaded on October 27,2025 at 12:44:51 UTC from IEEE Xplore. Restrictions apply.

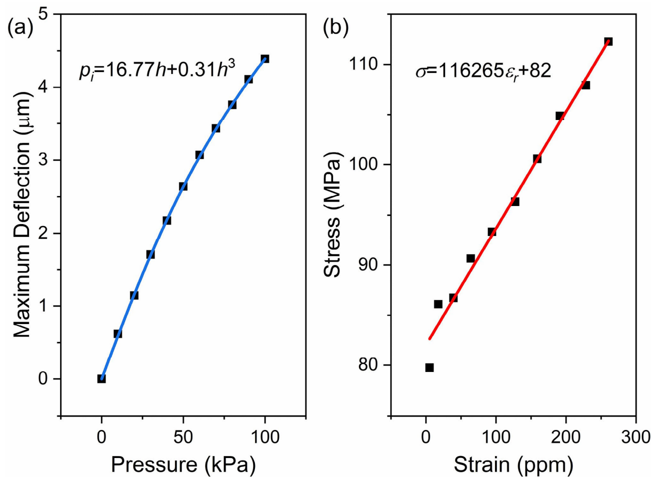

Fig. 7. (a) Maximum deflection of Si_3N_4/SiO_2 membrane from 0 to 100 kPa [the dots are the measured data from Fig. 6, the curve is the fit model of (9)]. (b) Stress-strain diagram at the membrane center [the dots are calculated data by (11) and (12), the line is the fit model of (13)].

over-etching of the membrane. The membrane stack can also be different at the edges due to the presence of the Si resistors and metal tracks. Due to these structural differences, the membrane edges might deform differently from the center part and should not be considered for further membrane deformation analysis. According to the topographies, the membrane area enclosing the four piezoresistors can be approximated as a circular shape with a radius (a) of 222 μm. Three-dimensionally, assuming a uniform applied pressure, the inner circular membrane would be deformed into a spherical cap as observed.

Three main components condition the elastic deformation: straining- and bending-induced stress caused by the applied pressure, as well as residual stress induced by the fabrication and packaging [29], [30]. Considering a much smaller membrane deflection (h) than the radius, the biaxial modulus (Y) related to the rigidity of elasticity and residual stress (σ_0) could be extracted by two classical models for thin-walled spherical pressure vessels. These models are both considered in the neutral plane of the thin membrane, where bending-induced stress is zero and only straining-induced stress and residual stress are considered.

First, considering the maximum deflection from 0 to 100 kPa, the pressure-deflection behaviors are obtained in Fig. 7(a). The maximum deflections are obtained by the height differences between the membrane center and the average position of resistor centers, after subtracting the initial membrane height at zero pressure. Based on the classical spherical model for a circular membrane, the data can be fit by "Cabrera's equation" [31]

$$p_i = 4\frac{t}{a^2}\sigma_0 h + \frac{8}{3}\frac{t}{a^4}Yh^3 \tag{9}$$

where t is the membrane thickness. This model assumes an equi-biaxial stress throughout the membrane, but the stress at the membrane edges is not equibiaxial due to the clamped boundary condition. Therefore, the calculated Y is expected to be lower than the actual biaxial modulus (Y_{act}) given by [32]

$$Y_{\text{act}} = \frac{Y}{1 - 0.24\upsilon_m - 0.00027(1-\upsilon_m)\sigma_0} \tag{10}$$

TABLE I

MECHANICAL RESULTS EXTRACTED BY DIFFERENT METHODS

Models	Y (GPa)	Y_{act} (GPa)	E (GPa)	σ_0 (MPa)
***h-p* fitting**	112.9	122.1	115	82.6
σ-ε fitting	116.3	123.5	116.3	82

where υ_m is the Poisson's ratio of the membrane stack. For the thin Si_3N_4/SiO_2 membrane without significant interfacial effect, υ_m of 0.242 is estimated by a weighted average of υ for SiO_2 and Si_3N_4. The measured h–p data in Fig. 7(a) aligns well with (9), using parameters extracted in Table I. At lower pressure, the maximum deflection increases linearly due to the dominant residual stress, consistent with the linear term in (9). As the applied pressure increases, the straining-induced stress becomes dominant, leading to a cubic relation as described by the cubic term in (9).

Second, stress (σ) versus radial strain (ε_r) at the membrane center are calculated in Fig. 7(b). Derived from the force equilibrium condition in the spherical cap, biaxial stress is obtained by [33]

$$\sigma = \frac{p_i a^2}{4ht}. \tag{11}$$

Radial strain (ε_r) of the membrane is defined as the ratio of arclength change to the original arclength [34]

$$\varepsilon_r = \frac{2}{3a^2}h^2 \tag{12}$$

where ε_r remains almost constant from the membrane center to the circumference, while the tangential strain (ε_t) monotonically decreases from an equal value of ε_r to zero [32]. Extracting the slope and σ-intercept from a linear fitting of $\sigma - \varepsilon_r$ data, the total biaxial stress in the neutral plane of a thin circular membrane is the sum of the residual stress (σ_0) and the radial stress generated by the membrane deflection [32], [34]

$$\sigma = Y \cdot \varepsilon_r + \sigma_0. \tag{13}$$

Similar to the first model, Y is corrected by [30]

$$Y_{\text{act}} = \frac{Y}{1 - 0.24\upsilon_m}. \tag{14}$$

The $\sigma - \varepsilon_r$ data are linearly fit with (13) in Fig. 7(b), using parameters extracted in Table I. The h–p and σ–ε_r models yield close Y_{act} of ~123 GPa. Assuming zero tangential strain throughout the membrane, Young's modulus (E) of plate-like membranes is calculated by $E_m = Y_{\text{act}}(1-\nu^2)$ [35]. Both models yield very close E_m and σ_0 of ~116 GPa and ~82 MPa. The mechanical elastic properties of the Si_3N_4/SiO_2 membrane analyzed by the two different models keep almost identical and consistent with E_m (120–160 GPa) and σ_0 (50–100 MPa) of Si_3N_4/SiO_2 membranes reported in [36]. Considering the maximum deformation of only 0.03%, the measured mechanical performances fit well with two different elastic models, which validate the elastic behavior of the membrane. Finite element simulations can be performed on the Si_3N_4/SiO_2 membrane in the future to more precisely understand the stress and strain distributions in both Si_3N_4 and SiO_2 layers, as well as at their interface.

Authorized licensed use limited to: Univ Catholique de Louvain/UCL. Downloaded on October 27,2025 at 12:44:51 UTC from IEEE Xplore. Restrictions apply.

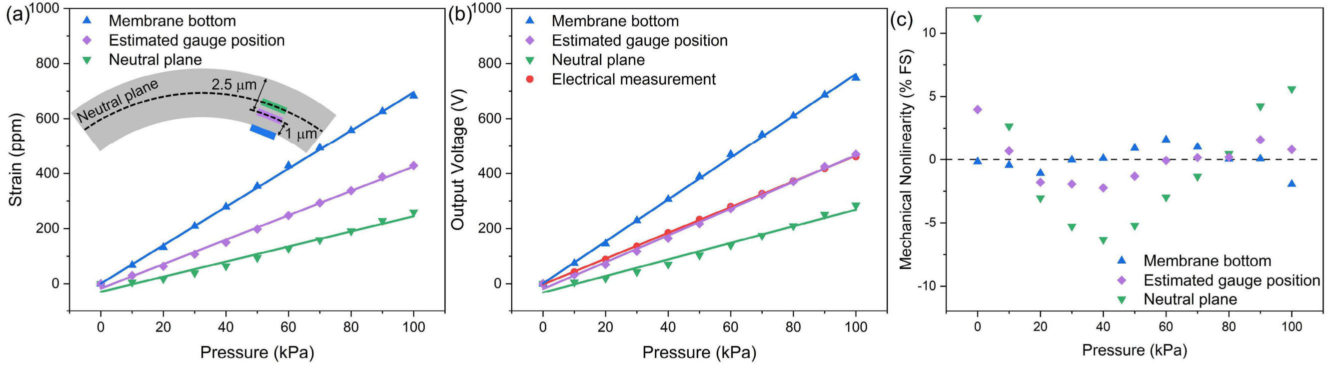

Fig. 8. (a) Strain in the membrane calculated by (15) using the experimental deflection data under pressure from Fig. 7(a), for three conditions: neutral plane ($C = 0$), estimated experimental gauge position ($C = 0.4$), and membrane bottom ($C = 1$), as shown in the inset of (a). Corresponding (b) output voltage and (c) mechanical nonlinearity errors of the pressure sensor calculated by (3) and (7) using the strain values of (a) from 0 to 100 kPa with a supply voltage of 10 V. The dots and lines represent the calculations and linear fittings, respectively. V_o obtained by electrical measurements in Fig. 4(e) is compared with the model in (b).

D. Discussion of Electromechanical Performance

Since the strain in the piezoresistors is converted into resistance variations, ultimately contributing to the electrical outputs, it is crucial to evaluate the strain in the piezoresistive gauges. As discussed in Section IV-C, the strain in the neutral plane of the membrane edge is predominantly radial and equal to the radius strain at the membrane center. However, the gauges fabricated in this work are not located in the neutral plane. The gauge center is 1 μm (= 0.5 μm Si + 0.5 μm SiO_2) and 2.5 μm (= 0.5 μm Si + 0.5 μm SiO_2 + 1.5 μm Si_3N_4) away from the bottom and top surfaces of the membrane, respectively. Equation (12) used in the neutral plane ignored the bending-induced radial strain, which should be added when the gauges are placed between the neutral plane and the membrane bottom, yielding

$$\varepsilon_r = \frac{2}{3a^2}h^2 - C\frac{t \cdot h}{a^2}\left(1 - 5e^{-S_f \frac{|h|}{a}}\right) \quad (15)$$

where S_f, the shape factor, equals 5 for nearly parabola-shaped thin membranes [37], and the coefficient C increases from 0 to 1 from the neutral fiber to the membrane bottom. In Fig. 8(a), ε_r is calculated by (15) using the experimental deflection data under pressure from Fig. 7(a) for two boundary conditions: the neutral plane ($C = 0$) and the membrane bottom ($C = 1$), as well as an estimated experimental gauge position ($C = 0.4$).

Using these calculated ε_r from Fig. 8(a), the radial and tangential stresses acting on the Si strain gauges could be calculated by [32] and [37]

$$\sigma_r = \frac{E_{\text{Si}}}{1 - \nu_{\text{Si}}^2}\varepsilon_r \quad (16)$$

$$\sigma_t = \nu_{\text{Si}}\sigma_r \quad (17)$$

where ν_{Si} and E_{Si}, the Poisson's ratio and Young's modulus of silicon, equal to 0.064 and 169 GPa for the [110] direction on the (100) Si [35]. In Fig. 8(b), V_o are calculated by incorporating the calculated σ_r and σ_t as $\sigma_\parallel$ and $\sigma_\perp$ into (3) and are compared with the electrical measurements from Fig. 4(e). At any pressure, V_o increases gradually if the strain gauges were moved from the neutral plane to the membrane bottom, thanks to an enhanced bending-induced strain.

However, precisely estimating the neutral plane and the strain distribution within the experimental membrane is challenging, since the membrane at the gauge position consists of multilayers with additional thick metal lines on the membrane edges to contact with the gauges. Supposing that C in (15) equals 0.4, V_o calculated by the model reveals a close fitting with the electrical measurement in Fig. 8(b). This empirical fit assumes that the gauges are in their as-fabricated positions, with the corresponding ε_r illustrated in Fig. 8(a).

The NL_M reported in Fig. 8(c) are calculated by (7) with the modeled data of Fig. 8(b). High NL_M are observed at the neutral plane, while the increased bending-induced strain compensates the NL_M as the gauges approach the membrane bottom. Compared to the NL_T in Fig. 4(f), the NL_M obtained at the gauge position show a similar tendency but higher values up to 3.98% FS. The total NL thus appears dominated by the mechanical NL compared to the electrical NL of only up to 0.25% FS obtained in Fig. 4(b). Additionally, nonsymmetrical piezoresistors and other uncertainties in the device and the measurements also contribute to the nonlinearity differences.

On the other hand, the same model is used to explain the behavior of the thin membrane undergoing a downward deformation under negative pressure. The first and second terms in (15) become negative and positive, respectively. In Fig. 6, the maximum deflection at −30 kPa is −1.53 μm. The straining-induced stress is −0.0032%, while the bending-induced stress increases from 0 to 0.015% from the neutral plane to the membrane bottom. As the negative pressure increases, the increase of the bending-induced stress would counteract the straining-induced stress acting on the gauges, ultimately leading to zero electrical output, explaining the reduced electrical performance in Fig. 4(c) and (d).

Finally, significantly higher S and FoM_m were achieved in this work compared to almost all the reported Si pressure sensors with larger or thicker membranes as summarized in [23]. The as-fabricated pressure sensor is compared with other reported Si piezoresistive Wheatstone-bridge pressure sensors featuring similar dimensions in Table II. Compared to the sensors with close areas but based on planar Si piezoresistors in bulk monocrystalline silicon technology [16] or SOI technology [6], this work achieved higher S and FoM_m. Such improvements are attributed to a thinner membrane, a gauge position closer to the membrane surface, and fabrication optimizations combining the advantages of SOI

Authorized licensed use limited to: Univ Catholique de Louvain/UCL. Downloaded on October 27,2025 at 12:44:51 UTC from IEEE Xplore. Restrictions apply.

TABLE II
COMPARISON WITH REPORTED SI PIEZORESISTIVE WHEATSTONE-BRIDGE PRESSURE SENSORS WITH SIMILAR DIMENSIONS

Substrate	Diaphragm	Piezoresistors	*A* (mm^2)	*t* (μm)	*Pressure Range* (kPa)	V_{dd} (V)	*S* (μV/V/Pa)	FOM_m (ppm/Pa/mm^2)	NL_T (% FS)
SOI [6]	Mono-Si	Planar mono-Si	0.3025	14	100	1	0.14	0.463	/
Bulk Si [16]	Mono-Si/SiO_2	Planar mono-Si	0.23	13.8	200	5	0.096	0.417	0.16
Bulk Si [20]	/	Mesa poly-Si	0.09	2	100	1	0.0548	0.609	0.1
Bulk Si with concentrators [22]	Poly-Si	Planar mono-Si	0.71	2	1.2	5	3.6	5.07	0.05
SOI (This work)	Si_3N_4/SiO_2	Mesa mono-Si	0.18	2.5	100	10	0.461	2.56	0.78

technology and mesa piezoresistors. Under the same pressure, thinner membranes are expected to have larger deflections according to (9). As shown in (15), higher deflections and a smaller membrane area are helpful to increase the gauge strain, ultimately contributing to an enhanced response. Based on the mesa polysilicon technology, a pressure sensor with similar dimensions [20] exhibited worse piezoresistive responses than this work but a higher FoM_m than [16] thanks to its smaller A and t. Nevertheless, favoring high S in this work leads to an NL_T higher than the other reported sensors. Such a high total NL is mainly caused by the mechanical NL of the strain induced on the Si gauges, that can be improved by placing the piezoresistors closer to the membrane bottom, as depicted in Fig. 8(c). Introducing concentrators in pressure sensors could also significantly improve the piezoresistive performance [22] and thus can be considered in the future work to enhance the sensitivity and limit the nonlinearity of pressure sensors.

V. CONCLUSION

In conclusion, this work investigates in-depth the electromechanical measurements and modeling of a small-area ultrathin SOI MEMS differential pressure sensor. To obtain stable output signals, a Wheatstone full-bridge structure was implemented with four monocrystalline Si mesa strain gauges at the edges of a Si_3N_4/SiO_2 membrane with a thickness of 2.5 μm and an area of 0.18 mm^2, to maximize its sensitivity and stabilize the electrical output.

The fabricated pressure sensor exhibits excellent electrical and mechanical performances under positive backside differential pressure from 0 to 100 kPa, both at 5 and 10 V supply voltages. Specifically, with $V_{dd} = 10$ V, the pressure sensor achieves a peak V_o of 461 mV, a S of 0.461 μV/V/Pa, and a FoM_m of 2.56 ppm/Pa/mm^2, respectively. The output voltage shows a linear tendency, indicating a stable sensitivity with increasing positive pressure and a maximum NL_T of 0.78% FS. The topographic measurements of the Si_3N_4/SiO_2 membrane analyzed by h–p and σ–ε_r models yield close values for Young's modulus and residual stress of $\sim$116 GPa and $\sim$82 MPa, respectively. The excellent electrical performance under positive pressure is attributed to the high strain increase with pressure at the gauge positions near the membrane edges and close to the membrane bottom. Considering a much lower electrical NL of the Wheatstone bridge, a relatively high total NL is dominated by the mechanical NL, that is, nonlinear strain variation acting on gauges with pressure.

Conversely, the electrical performance of the pressure sensor degrades with increasing negative pressure and no signal was detected below −30 kPa. At −30 kPa, the pressure sensor shows reduced S and FoM_m of 0.283 μV/V/Pa and 1.57 ppm/Pa/mm^2 and a much higher NL_T of 4% FS with $V_{dd} = 10$ V. These results are attributed to the negative impact from the bending-induced strain on the electrical output. As a result, the pressure sensor is optimally operated under positive backside differential pressure from 0 to 100 kPa, with excellent electrical and mechanical performances. In the future, to reach higher sensitivity and lower nonlinearity simultaneously in either upward or downward deformation, strain gauges should be integrated closer to the membrane surface or stress concentrators should be employed.

REFERENCES

[1] S. Liu, H. Liang, and B. Xiong, "An out-of-plane electromagnetic induction based resonant MEMS magnetometer," *Sens. Actuators A, Phys.*, vol. 285, pp. 248–257, Jan. 2019.

[2] F. Khoshnoud and C. W. de Silva, "Recent advances in MEMS sensor technology-mechanical applications," *IEEE Instrum. Meas. Mag.*, vol. 15, no. 2, pp. 14–24, Apr. 2012.

[3] M. Chen et al., "An ultrahigh resolution pressure sensor based on percolative metal nanoparticle arrays," *Nature Commun.*, vol. 10, no. 1, Sep. 2019, Art. no. 4024.

[4] K. Singh, R. Joyce, S. Varghese, and J. Akhtar, "Fabrication of electron beam physical vapor deposited polysilicon piezoresistive MEMS pressure sensor," *Sens. Actuators A, Phys.*, vol. 223, pp. 151–158, Mar. 2015.

[5] E. L. W. Gardner, A. De Luca, J. Philippe, D. Dragomirescu, and F. Udrea, "Thin-film MOSFET-based pressure sensor," *IEEE Sensors Lett.*, vol. 3, no. 7, pp. 1–4, Jul. 2019.

[6] Y. Guo et al., "Stand-alone stretchable absolute pressure sensing system for industrial applications," *IEEE Trans. Ind. Electron.*, vol. 64, no. 11, pp. 8739–8746, Nov. 2017.

[7] G. Pillai, A. A. Zope, J. M.-L. Tsai, and S.-S. Li, "Piezoelectric MEMS resonators: A review," *IEEE Sensors J.*, vol. 21, no. 11, pp. 12589–12605, Jun. 2021.

[8] R. d. S. Pereira and C. A. Cima, "Thermal compensation method for piezoresistive pressure transducer," *IEEE Trans. Instrum. Meas.*, vol. 70, pp. 1–7, 2021.

[9] A. V. Tran, X. Zhang, and B. Zhu, "The development of a new piezoresistive pressure sensor for low pressures," *IEEE Trans. Ind. Electron.*, vol. 65, no. 8, pp. 6487–6496, Aug. 2018.

[10] S. S. Kumar and B. D. Pant, "Design principles and considerations for the 'ideal' silicon piezoresistive pressure sensor: A focused review," *Microsyst. Technol.*, vol. 20, no. 7, pp. 1213–1247, Jul. 2014.

[11] V. Pandey, A. Mandal, S. Sisle, M. P. Gururajan, and R. O. Dusane, "Piezoresistive pressure sensor using nanocrystalline silicon thin film on flexible substrate," *Sens. Actuators A, Phys.*, vol. 316, Dec. 2020, Art. no. 112372.

[12] C. Zhou, Y. Zhang, B. Zheng, W. Xue, and Q. Wang, "Effect of internal stress on nonlinearity and sensitivity of a pressure sensor with SiN composite diaphragm," *Phys. Lett. A*, vol. 381, no. 4, pp. 284–291, Jan. 2017.

[13] X. Huang and D. Zhang, "A high sensitivity and high linearity pressure sensor based on a peninsula-structured diaphragm for low-pressure ranges," *Sens. Actuators A, Phys.*, vol. 216, pp. 176–189, Sep. 2014.

[14] E. K. Sackmann, A. L. Fulton, and D. J. Beebe, "The present and future role of microfluidics in biomedical research," *Nature*, vol. 507, no. 7491, pp. 181–189, Mar. 2014.

Authorized licensed use limited to: Univ Catholique de Louvain/UCL. Downloaded on October 27,2025 at 12:44:51 UTC from IEEE Xplore. Restrictions apply.

[15] A. Nisar, N. Afzulpurkar, B. Mahaisavariya, and A. Tuantranont, “MEMS-based micropumps in drug delivery and biomedical applications,” *Sens. Actuators B, Chem.*, vol. 130, no. 2, pp. 917–942, Mar. 2008.
[16] C. Gao, X. Hua, and D. Zhang, “Design and analysis of high-performance and small-size piezoresistive pressure sensors,” *IEEE Sensors J.*, vol. 23, no. 7, pp. 6649–6659, Apr. 2023.
[17] M. Basov and D. M. Prigodskiy, “Investigation of high-sensitivity piezoresistive pressure sensors at ultra-low differential pressures,” *IEEE Sensors J.*, vol. 20, no. 14, pp. 7646–7652, Jul. 2020.
[18] M. Basov, “Ultra-high sensitivity MEMS pressure sensor utilizing bipolar junction transistor for pressures ranging from -1 to 1 kPa,” *IEEE Sensors J.*, vol. 21, no. 4, pp. 4357–4364, Feb. 2021.
[19] F. Xue et al., “Piezoelectric-piezoresistive coupling MEMS sensors for measurement of electric fields of broad bandwidth and large dynamic range,” *IEEE Trans. Ind. Electron.*, vol. 67, no. 1, pp. 551–559, Jan. 2020.
[20] C. H. Je, S. Q. Lee, and W. S. Yang, “High sensitivity surface micromachined absolute pressure sensor,” *Proc. Eng.*, vol. 168, pp. 725–728, Jan. 2016.
[21] D. Kanekal and S. K. Jindal, “Optimizing piezoresistive MEMS pressure sensor on a double cross beam silicon diaphragm with statistical curve-fitting and optimization techniques,” *IEEE Sensors J.*, vol. 24, no. 1, pp. 169–176, Jan. 2024.
[22] H. Zou, J. Wang, and X. Li, “High-performance low-range differential pressure sensors formed with a thin-film under bulk micromachining technology,” *J. Microelectromech. Syst.*, vol. 26, no. 4, pp. 879–885, Aug. 2017.
[23] T. P. Delhaye, N. André, L. A. Francis, and D. Flandre, “New universal figure of merit for embedded Si piezoresistive pressure sensors,” *IEEE Sensors J.*, vol. 21, no. 1, pp. 213–221, Jan. 2021.
[24] Y. Kanda, “A graphical representation of the piezoresistance coefficients in silicon,” *IEEE Trans. Electron Devices*, vol. ED-29, no. 1, pp. 64–70, Jan. 1982.
[25] C. S. Smith, “Piezoresistance effect in germanium and silicon,” *Phys. Rev.*, vol. 94, no. 1, pp. 42–49, Apr. 1954.
[26] N. André et al., “Ultra-low-power SOI-CMOS pressure sensor based on orthogonal PMOS gauges,” in *Proc. 12th IMEKO TC4 Int. Symp. 20th Int. Workshop ADC Modeling Test.*, Sep. 2017, pp. 1–12.
[27] T. Li, H. Xue, and W. Wang, “A high-pressure sensor with high linearity with S-shaped piezoresistors,” *IEEE Sensors J.*, vol. 23, no. 2, pp. 1052–1059, Jan. 2023.
[28] Y. Huang, X. Fan, S.-C. Chen, and N. Zhao, “Emerging technologies of flexible pressure sensors: Materials, modeling, devices, and manufacturing,” *Adv. Funct. Mater.*, vol. 29, no. 12, Mar. 2019, Art. no. 1808509.
[29] E. Masarweh, M. Arseenko, P. Guaino, and D. Flandre, “Membrane-based mechanical characterization of screen-printed inks: Deflection analysis of ink layers on polyimide membranes,” *Appl. Res.*, vol. 3, no. 4, Aug. 2024, Art. no. e202300113.
[30] S. Rosset, M. Niklaus, P. Dubois, and H. R. Shea, “Metal ion implantation for the fabrication of stretchable electrodes on elastomers,” *Adv. Funct. Mater.*, vol. 19, no. 3, pp. 470–478, Feb. 2009.
[31] J. Y. Pan, P. Lin, F. Maseeh, and S. D. Senturia, “Verification of FEM analysis of load-deflection methods for measuring mechanical properties of thin films,” in *IEEE 4th Tech. Dig., Solid-State Sensor Actuator Workshop*, Jan. 1990, pp. 70–73.
[32] M. K. Small and W. D. Nix, “Analysis of the accuracy of the bulge test in determining the mechanical properties of thin films,” *J. Mater. Res.*, vol. 7, no. 6, pp. 1553–1563, Jun. 1992.
[33] K. Nakagawa, K. Satoh, S. Murakami, K. Takei, S. Akita, and T. Arie, “Controlling the thermal conductivity of multilayer graphene by strain,” *Sci. Rep.*, vol. 11, no. 1, Oct. 2021, Art. no. 19533.
[34] H. Schlicke, E. W. Leib, A. Petrov, J. H. Schröder, and T. Vossmeyer, “Elastic and viscoelastic properties of cross-linked gold nanoparticles probed by AFM bulge tests,” *J. Phys. Chem. C*, vol. 118, no. 8, pp. 4386–4395, Feb. 2014.
[35] M. A. Hopcroft, W. D. Nix, and T. W. Kenny, “What is the young’s modulus of silicon?” *J. Microelectromech. Syst.*, vol. 19, no. 2, pp. 229–238, Apr. 2010.
[36] P. Martins, P. Delobelle, C. Malhaire, S. Brida, and D. Barbier, “Bulge test and AFM point deflection method, two technics for the mechanical characterisation of very low stiffness freestanding films,” *Eur. Phys. J. Appl. Phys.*, vol. 45, no. 1, p. 10501, Jan. 2009.
[37] W. K. Schomburg, *Introduction to Microsystem Design*, 2nd ed., Berlin, Germany: Springer, 2015.

Xi Zeng received the B.E. degree in electronic science and technology and the M.E. degree in integrated circuit engineering from Hunan University, Changsha, China, in 2016 and 2018, respectively, and the Ph.D. degree in electrical engineering with a focus on p-type optoelectronic devices from UCLouvain, Ottignies-Louvain-la-Neuve, Belgium, in 2022.

He is currently a Post-Doctoral Researcher at UCLouvain, on spiking sensors. His research interests include microelectromechanical system (MEMS) pressure sensors, thin-film transistors, and optoelectronic devices.

Nicolas André (Member, IEEE) received the M.S. degree in electrical engineering and the Ph.D. degree in applied sciences with a focus on the microelectromechanical system (MEMS) co-integration from UCLouvain, Ottignies-Louvain-la-Neuve, Belgium, in 2004 and 2011, respectively.

From 2011 to 2012, he was a Post-Doctoral Researcher at UdeS, Sherbrooke, QC, Canada, on improving LED efficiency. He has co-authored over 150 research articles and holds four patents. He has contributed to several Walloon, FEDER, and EU projects. His expertise lies in microfabrication and sensors integrated with SOI CMOS circuits.

Eléonore Masarweh was born in Belgium, in 1997. She received the M.S. degree in electromechanical engineering with a focus on the mechanical aspects of microelectromechanical system (MEMS) membranes from UCLouvain, Ottignies-Louvain-la-Neuve, Belgium, in 2021, where she is currently pursuing the Ph.D. degree in MEMS, membrane-based pressure sensors and flexible electronics.

Ottilie Bonfanti was born in Belgium, in 2000. She received the M.S. degree from UCLouvain, Ottignies-Louvain-la-Neuve, Belgium, in 2023, where she is currently pursuing the Ph.D. degree with the Institute of Information and Communication Technologies, Electronics and Applied Mathematics (ICTEAM).

Her research interests include microelectromechanical system (MEMS), sensor systems, radiation hardening, and SHM for space applications.

Denis Flandre (Senior Member, IEEE) received the M.S. degree in electrical engineering and the Ph.D. degree in applied sciences from UCLouvain, Ottignies-Louvain-la-Neuve, Belgium, in 1986 and 1990.

Since 2001, he has been a full-time Professor at UCLouvain. His Ph.D. research was on the modeling of silicon-on-insulator (SOI) MOS devices for characterization and circuit simulation, his post-doctoral thesis on a systematic and automated synthesis. He is involved in the research and development of SOI MOS devices, digital and analog circuits, as well as sensors, microelectromechanical system (MEMS) and photovoltaic cells, for special applications, more specifically low-voltage low-power, microwave, biomedical, radiation-hardened, and high-temperature electronics and microsystems. He has authored or co-authored more than 1200 technical papers or conference contributions, and 12 patents. He has organized or lectured many short courses on SOI technology, devices, and circuits in universities, industry, and conferences.

Authorized licensed use limited to: Univ Catholique de Louvain/UCL. Downloaded on October 27,2025 at 12:44:51 UTC from IEEE Xplore. Restrictions apply.